Separation of emission mechanisms in spintronic terahertz emitters

Yongshan Liu,[1,2,*] Houyi Cheng,[1,2,*] Yong Xu,[1,2,†] Pierre Vallobra,[2] Sylvain Eimer,[2] Xiaoqiang Zhang,[2] Xiaojun Wu,[3] Tianxiao Nie,[1] and Weisheng Zhao[1,2,‡]

[1]*MIIT Key Laboratory of Spintronics, School of Integrated Circuit Science and Engineering, Beihang University, Beijing 100191, China*

[2]*Hefei Innovation Research Institute, Beihang University, Hefei 230013, China*

[3]*School of Electronic and Information Engineering, Beihang University, Beijing, 100191, China*

(Received 22 March 2021; accepted 19 July 2021; published 9 August 2021)

Spintronic thin films were shown to be promising high-performance broadband terahertz (THz) emitters. For spintronic ferromagnet/heavy metal heterostructures, THz emission arises from three mechanisms: the magnetic dipolar radiation due to the ultrafast demagnetization, the transient current radiation due to spin-charge conversion, and anomalous Hall effect. Here, we demonstrate that the three mechanisms show distinct dependences on the thickness of the ferromagnetic layer. With the insertion of an ultrathin Al_2O_3 layer between the ferromagnetic and heavy metal layer, the spin-charge conversion is suppressed when the Al_2O_3 thickness exceeds 1 nm. Our results agree with the theoretical predictions based on a simple spin-diffusion model.

DOI: 10.1103/PhysRevB.104.064419

I. INTRODUCTION

Since the discovery of the ultrafast demagnetization in Ni by Beaurepaire *et al.* [1], the interaction between femtosecond laser pulses and magnetic materials has allowed magnetic moments to be manipulated on the subpicosecond timescale [2–4]. This discovery brings the speed of the spintronic devices to terahertz (THz) frequencies [5]. In 2004, Beaurepaire *et al.* reported that the ultrafast demagnetization in Ni results in the emission of a THz pulse proportional to the second derivative of the magnetization (d^2M/dt^2) [6]. This phenomenon is explained with Maxwell's electromagnetic theory by considering a time-dependent magnetic dipole. Although the magnetic dipole radiation cannot be considered an efficient THz radiation mechanism, the THz spectrum is still of great significance for revealing ultrafast spin dynamics of ferromagnets [7], ferrimagnets [8], and even antiferromagnets [9]. Recently, Huang *et al.* [10] experimentally investigated the THz emission behaviors in thick Co films and confirmed a direct relation between the THz emission and the photoinduced magnetization dynamics.

Kampfrath *et al.* proposed a different spintronic THz emission mechanism through spin-charge conversion (SCC) [11,12]. It is demonstrated that the ultrafast spin current could be effectively converted into an ultrafast charge current at the ferromagnet/heavy metal interface or in the bulk of the heavy metal layer. Femtosecond laser heating excites superdiffusive spin-polarized hot electrons in the ferromagnet layer [13–16]. In the presence of an adjacent heavy metal layer with strong spin-orbit coupling, the spin-polarized hot electrons diffuse into the heavy metal layer and form an ultrafast spin current that flows in the normal direction of the film plane [17–19]. Later, various types of materials with strong spin-orbit coupling were studied, such as heavy metals [20,21], Rashba interfaces [22,23], and topological insulators [24], etc. The ultrafast spin current can be converted to an ultrafast charge current via SCC mechanisms, such as the inverse Edelstein effect or the inverse spin Hall effect [25–27]. For ferromagnet/heavy metal bilayers, Huisman *et al.* demonstrated the helicity-dependent THz emission, which results from a helicity-dependent femtosecond laser-induced rotation of the ferromagnet magnetization [28,29]. The SCC mechanism dramatically enhances the THz emissions from spintronic THz emitters.

More recently, Zhang *et al.* demonstrated the THz emission from a single-layer ferromagnet via the anomalous Hall effect (AHE) [30]. For metallic ferromagnet films, hot electrons are reflected at the ferromagnet/dielectric interface to form backflow nonthermal charge currents. The backflow currents from the two interfaces are not completely canceled out, leading to a net backflow current. The backflow current is converted to a transverse transient charge current via the AHE.

Although the three THz radiation mechanisms have been proposed independently to explain the spintronic THz emission, a direct comparison of these mechanisms is still lacking. This paper presents a systematic study of the THz radiation generated from the three emission mechanisms. The paper is organized as follows: the samples and the experimental setup are described in Sec. II. In Sec. III, we present the role of the Al_2O_3 buffer layer, the ferromagnet thickness dependence for the three THz emission mechanisms, and the effect of a thin Al_2O_3 insertion layer. In Sec. IV, we analyze the magnetic dipole contribution and the SCC contribution from typical ferromagnet/heavy metal spintronic THz emitters quantitatively.

*These authors contributed equally to this work.

†yongxu@buaa.edu.cn

‡weisheng.zhao@buaa.edu.cn

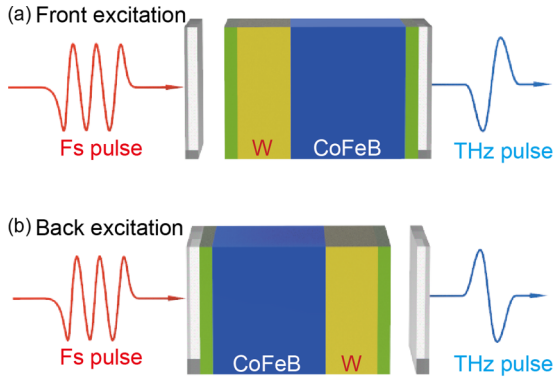

FIG. 1. Schematic of a spintronic bilayer Al_2O_3 (1 nm)/CoFeB (8 nm)/W (4 nm)/Al_2O_3 (3 nm) grown on glass substrates. The near-infrared laser is incident on the film side: (a) front excitation or the substrate side (b): back excitation).

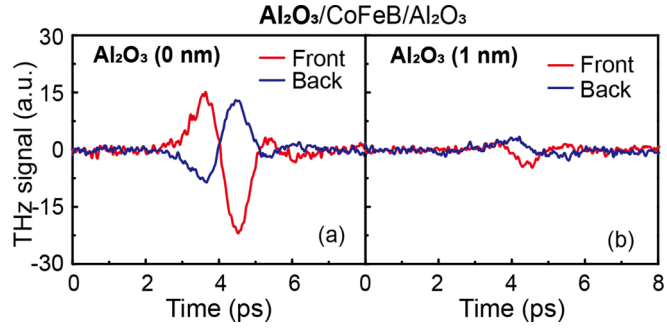

FIG. 2. THz waveforms from glass//CoFeB (8 nm)/Al_2O_3 (3 nm) (a) and glass//Al_2O_3 (1 nm)/CoFeB (8 nm)/Al_2O_3 (3 nm) (b) heterojunctions with front and back excitations.

II. METHODS

In this study, the following four series of samples have been prepared by magnetron sputtering on glass substrates:

Series 1: W (4 nm)/CoFeB (1, 2, 4, 8, 16 nm)/MgO (1 nm)/Ta (2 nm)

Series 2: Al_2O_3 (1 nm)/CoFeB (2, 4, 8, 16 nm)/Al_2O_3 (3 nm)

Series 3: Al_2O_3 (1 nm)/CoFeB (8 nm)/Al_2O_3 (0–4 nm)/W (4 nm)/Al_2O_3 (3 nm)

Series 4: Al_2O_3 (1 nm)/CoFeB (8 nm)/Al_2O_3 (0–4 nm)/Pt (4 nm)/Al_2O_3 (3 nm)

For all the samples, Al_2O_3 (1 nm) and Al_2O_3 (3 nm) serve as the buffer layer and the capping layer, respectively. The role of Al_2O_3 (1 nm) will be further discussed in Sec. III A. All the CoFeB layers show an in-plane magnetic anisotropy. Atomic force microscopy (AFM) analysis shows that the thin-film roughness is less than 0.8 nm (see Fig. 7 in Appendix A).

The THz emission spectra were carried out in a home-built THz time-domain spectrometer. During the whole experiment, a static in-plane field of 1000 Oe is applied to fix the CoFeB magnetization. A femtosecond laser pulse is generated by an amplified Ti:sapphire laser with a central wavelength of 800 nm, a pulse duration of 35 fs, and a repetition rate of 1 kHz. We use a fluence of $\sim 0.42\,\mathrm{mJ/cm^2}$ to pump the spintronic THz emitter, and the THz pulse is detected with a 2-mm-thick ZnTe crystal via electro-optical sampling. When the pumped laser is incident from the film (substrate) side, it is referred to as front- (back-)side excitation. [Figs. 1(a) and 1(b)]. We add another glass substrate in front of the film to minimize the impact of the substrate on the THz signal. The humidity is lower than 2% during all the measurements.

III. RESULTS

A. Emission mechanisms in single CoFeB layer

We first investigate the THz emission from a single ferromagnet layer. Figure 2(a) shows the THz signals generated from Glass//CoFeB (8 nm)/Al_2O_3 (3 nm) without an Al_2O_3 buffer layer. We observe opposite waveform polarities with front and back excitations. After inserting a thin Al_2O_3 layer between the CoFeB layer and the glass substrate, the THz signal is greatly reduced, and the waveform polarities are the same for front and back excitations [Fig. 2(b)]. We observe similar THz waveforms for the thickness of the Al_2O_3 buffer layer ranging between 1 and 3 nm (data not shown).

The THz emission strongly depends on the two CoFeB/dielectric interfaces, which agrees with the AHE-induced THz emission in single-layer ferromagnets proposed by Zhang *et al.* In the absence of the thin Al_2O_3 layer, the two interfaces of CoFeB are asymmetric. The backflow currents from the two interfaces will not be canceled out due to the two different interfaces, leading to a net backflow current. The net backflow current is then converted to a transverse transient charge current via the AHE. After inserting a thin Al_2O_3 buffer layer, the two interfaces of CoFeB are similar, leading to a reduced net backflow current. It should be noted that even in the case of symmetric interfaces such as Al_2O_3/CoFeB/Al_2O_3, the bottom interface is smoother than the upper interface. Therefore, the net backflows cannot be fully compensated. The AHE radiation should always exist in single-layer CoFeB.

Moreover, the ultrafast demagnetization of CoFeB can be described as a time-dependent magnetic dipole, leading to magnetic dipole radiation. According to the electromagnetic theory, magnetic dipole radiation depends solely on magnetization dynamics. Because the ultrafast demagnetization dynamics are similar for both the front and back excitations, THz waveform polarities are expected to be the same, which agrees with the results in Fig. 2(b).

B. CoFeB thickness dependences for THz emission mechanisms

Figure 3(a) shows THz waveforms from CoFeB (16 nm) with front and back excitations. We identify a clear loss in amplitude for back in comparison to front excitation. This can be understood by considering the waveform polarities driven by AHE and magnetic dipole effect. In the case of front excitation, the waveform polarities are the same for the two mechanisms, resulting in an enhanced THz signal; in the case of back excitation, the waveform polarities are different for the two mechanisms, and the total THz signal is reduced.

For further clarifying the two mechanisms in single-layer CoFeB, we analyzed the THz emission as a function of CoFeB thickness. Figure 3(b) shows the waveforms from front

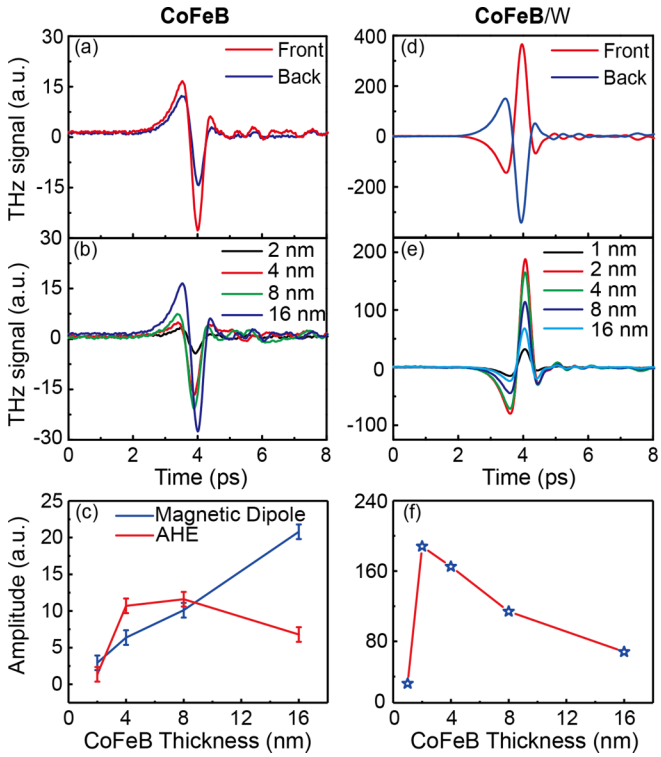

FIG. 3. (a) THz waveforms from CoFeB (16 nm) without any heavy metal layer with front and back excitations. (b) THz waveforms from CoFeB (2, 4, 8, and 16 nm) with front excitation. (c) The peak amplitudes are extracted at 4 ps for front and back excitations. The average (magnetic dipole) and the difference (AHE) are calculated and plotted as a function of the CoFeB thickness. (d) THz waveforms from CoFeB (8 nm)/W (4 nm) with front and back excitations. (e) THz waveforms from W (4 nm) /CoFeB (1, 2, 4, 8, and 16 nm). (f) The peak amplitudes are extracted at 4 ps and are plotted as a function of the CoFeB thickness. The buffer layer Al_2O_3 (1 nm) and the capping layer Al_2O_3 (3 nm) are omitted for simplicity.

excitation. (Back excitation results are not shown.) The peak amplitudes of THz waveforms are extracted at 4 ps for front and back excitation. Considering the waveform polarity for the two mechanisms, we conclude that the average and the difference correspond to the magnetic dipole contribution and the AHE contribution, respectively. The magnetic dipole contribution and the AHE contribution are shown as functions of CoFeB thickness in Fig. 3(c). For the magnetic dipole contribution, the THz signal increases monotonically with the CoFeB thickness, which can be explained because the magnetic dipole field increases as the CoFeB thickness increases. For the AHE contribution, the THz emission reaches its maximum value at ∼6 nm of CoFeB and then decreases gradually, which is consistent with the result reported by Zhang *et al.* [30].

Figure 3(d) shows the THz signals generated from CoFeB (8 nm)/W (4 nm) with front and back excitations. The polarity of the emitted THz pulses reverses when the pump beam is incident on the opposite side of the heterostructure. The opposite polarities indicate that the in-plane charge currents have a 180° phase shift in oscillations of the transient charge pulse. According to the SCC mechanism [11], the transient charge currents generated by inverse spin-Hall effect $j_c \propto j_s \times \sigma$, where j_c is the charge current, j_s is the spin current, and σ is the direction of the spin polarization. By pumping in the opposite direction, the ultrafast spin current j_s flows in the opposite direction and reverses the polarity of the ultrafast charge current j_c [31,32].

Figure 3(e) shows the waveforms from W (4 nm)/CoFeB (1, 2, 4, 8, 16 nm). The peak amplitudes of THz waveforms are extracted at 4 ps and plotted as a function CoFeB thickness. [Fig. 3(f)] The THz emission reaches its maximum value at 2 nm of CoFeB, which is similar to previous studies [21]. The thickness dependence is related to the laser-induced spin diffusion and the optical absorption in the ferromagnet layer [33,34]. (See Sec. IV and Fig. 9 in Appendix C for the spin-diffusion calculation.)

C. CoFeB/Al_2O_3/heavy metal

The THz emission should arise from the three mechanisms in a typical spintronic THz emitter based on the ferromagnet/heavy metal heterostructure. The THz signal due to the SCC is usually much stronger than the other mechanisms. To distinguish the three emission mechanisms, we insert a thin Al_2O_3 layer between the heavy metal layer and the CoFeB layer. The spin current reaching the heavy metal layer can be effectively controlled by varying the thickness of the Al_2O_3 layer.

Figure 4(a) shows the THz waveform of CoFeB (8 nm)/Al_2O_3 (0.9 nm)/W (4 nm). The THz waveforms show clear asymmetry for front and back excitations: the signal from the front excitation is much smaller than that of back excitation. It has been shown that the waveform polarity from magnetic dipole radiation remains the same for front and back excitations, while the waveform polarity from the other contributions, i.e., the contributions due to anomalous Hall effect and spin-charge conversion, become the opposite. Therefore, we are able to decompose the two waveforms in Figs. 4(b) and 4(c) into the average part (the magnetic dipole contribution, pink dashed lines) and the difference part (the SCC contribution and the AHE contribution, green dashed lines). Similarly, The THz waveform obtained from CoFeB (8 nm)/Al_2O_3 (0.9 nm)/Pt (4 nm) are asymmetric for front and back excitation [Fig. 4(d)]. In Figs. 4(e) and 4(f), the two waveforms are decomposed into the average part (the magnetic dipole contribution, pink dashed lines) and the difference part (the SCC contribution and the AHE contribution, green dashed lines).

We notice that the average part in Fig. 4, which stands for the magnetic dipole contribution, is more or less the same for the two samples and/or the two excitation directions. However, the difference part depends on the competition between the SCC contribution and the AHE contribution. Note the waveform polarities are different for the two samples, because the signs of the spin Hall angle are different for W and Pt.

To tune the intensity of the THz signal arising from SCC, we vary the thickness of the Al_2O_3 insertion layer in CoFeB/Al_2O_3/W and CoFeB/Al_2O_3/Pt. The peak intensities are plotted as a function of the thickness of the Al_2O_3 insertion layer in Figs. 5(a) and 5(b). When the Al_2O_3 layer is very thin,

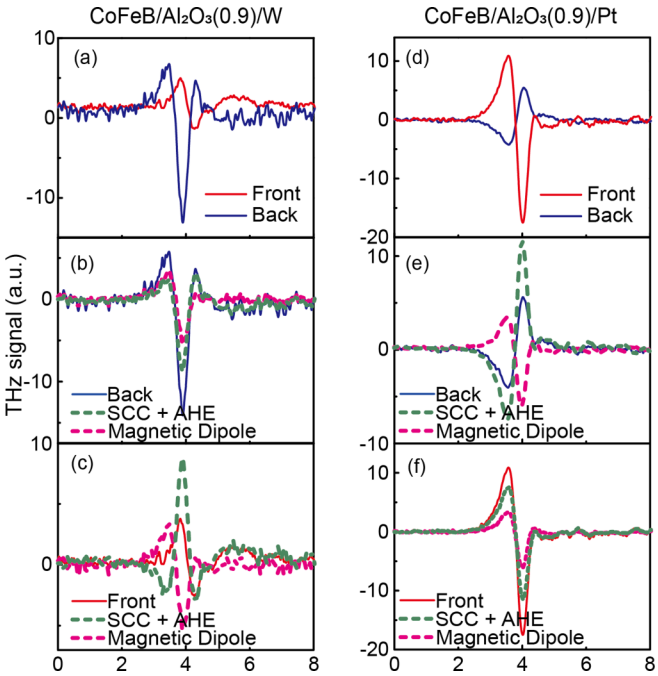

FIG. 4. (a) THz waveforms from CoFeB (8 nm)/Al_2O_3 (0.9 nm)/W (4 nm) with the front and back excitations. For the case of back excitation (b) and front excitation (c), the total signal is decomposed into a superposition of the difference part (green dashed line, SCC and AHE contributions) and the average part (pink dashed line, magnetic dipole contribution). (d) THz waveforms from CoFeB (8 nm)/Al_2O_3 (0.9 nm)/Pt (4 nm). The difference part and the average part are shown for the back (e) and front (f) excitations. The buffer layer Al_2O_3 (1 nm) and the capping layer Al_2O_3 (3 nm) are omitted for simplicity.

it is discontinuous, and the spin current is able to propagate through the pinholes of the Al_2O_3 layer. As the thickness of the Al_2O_3 layer increases, the intensity of THz signals decreases gradually since the amplitude of the transient spin current is related to the thickness of the Al_2O_3 insertion layer. When the thickness of the Al_2O_3 layer approaches ~0.9 nm, the Al_2O_3 layer becomes continuous and blocks the spin current at the ferromagnet/heavy metal interface.

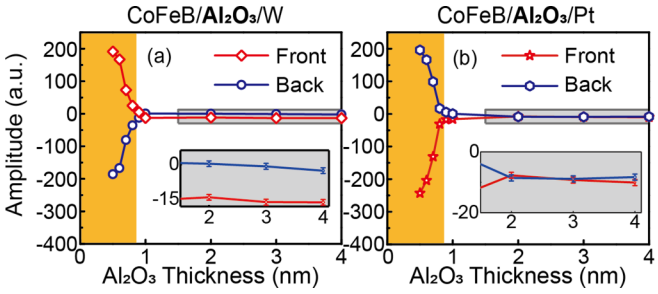

FIG. 5. (a) Peak intensity is shown as a function of the Al_2O_3 thickness for CoFeB (8 nm)/Al_2O_3 (x nm)/W (4 nm). (b) The peak intensity is shown as a function of the Al_2O_3 thickness for CoFeB (8 nm)/Al_2O_3 (x nm)/Pt (4 nm). The buffer layer Al_2O_3 (1 nm) and the capping layer Al_2O_3 (3 nm) are omitted for simplicity.

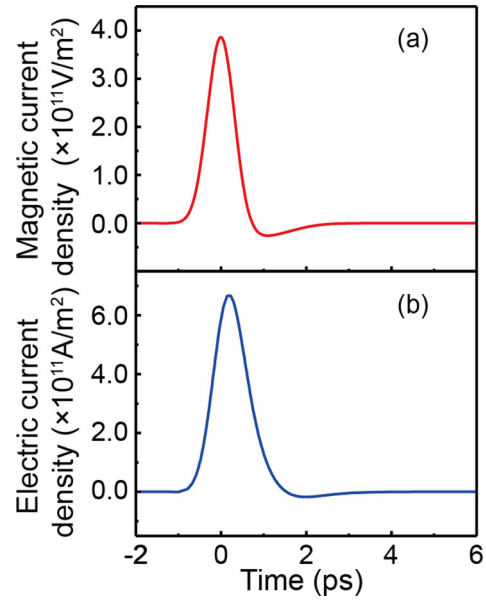

FIG. 6. Magnetic current density (a) and electric current density (b) are shown as a function of time. The current densities are averaged over the total film thickness.

The insets of Fig. 5 show the peak amplitude variation with the Al_2O_3 thickness above 1 nm. In the inset of Fig. 5(a), we observe both the magnetic dipole effect and AHE for the sample CoFeB/Al_2O_3/W, which is consistent with the previous results of a single CoFeB layer [Fig. 3(c)]. However, for CoFeB/Al_2O_3/Pt, the magnetic dipole contribution remains the same while the AHE contribution disappears [inset of Fig. 5(b)]. It might be due to some structural change at the CoFeB interfaces after the deposition of the Pt layer.

IV. DISCUSSION

In this section, we present a quantitative analysis for the THz emission mechanisms. For the THz emission via AHE, the current pulse cannot be easily evaluated because it strongly depends on the interfacial properties. For the magnetic dipole radiation and SCC-type radiation, the driving sources are ultrafast magnetic current pulses and ultrafast electric current pulses, respectively. According to the electromagnetism theory, an electric dipole and a magnetic dipole can be described *as* Il and Kl, respectively, where I is the electric current, K is the magnetic current, and l the length of the two dipoles. Assuming the oscillation frequencies of the two dipoles are the same, the ratio of the electric dipole field and the magnetic dipole field follows $\eta I/K$, where η is the free-space impedance.

For the magnetic dipole radiation, the magnetic current is triggered by time-dependent magnetization. [Fig. 6(a)] The magnetic current density can be evaluated using the ultrafast demagnetization curve (Fig. 8 in Appendix B). For the laser fluence used in this study (0.42 mJ/cm^2), we observe 40% demagnetization, which corresponds to a peak magnetic current density of 3.8×10^{11} V/m^2.

For the SCC-type radiation, we qualitatively analyze the spin-current density and the SCC in the heavy metal layer.

For simplicity, we use a spin-diffusion model to describe the spin diffusion in the ferromagnet/heavy metal heterostructure. Note that the spin-diffusion model neglects the transport of superdiffusive hot electrons. For a more accurate description below several hundreds of picoseconds, one needs to solve the Boltzmann equation to include the transport of spin-polarized hot electrons [18]. The spin-diffusion equation is given as follows:

$$\frac{\partial \mu_s}{\partial t} = D\frac{\partial^2 \mu_s}{\partial z^2} - \frac{\mu_s}{\tau_s} + \frac{g_s}{\mu_B N_F},$$

where $\mu_s = \mu_\uparrow - \mu_\downarrow$ is the spin chemical potential, D is the spin-diffusion constant, τ_s is the spin-relaxation time, $g_s = -dM/dt$ is the spin generation rate, μ_B is the Bohr magnetron, and N_F is the electron density of states. The D of Pt and CoFeB are 200 and 100 $\mathrm{nm}^2/\mathrm{ps}$, while the τ_s of Pt and CoFeB are 0.5 and 0.1 ps, respectively [15]. The spin generation rate is obtained from the ultrafast demagnetization dynamics, which are measured using the time-resolved magneto-optical Kerr effect. The charge current can be obtained by using the spin Hall angle $\gamma \sim \pm 0.05$ [35]. Our calculation shows that the peak charge current density reaches $7 \times 10^{11}\mathrm{A/m}^2$. [Fig. 6(b)] Therefore, the ratio between SCC radiation and magnetic dipole radiation is estimated to be $\eta I/K \sim 33$, which is consistent with the experimental data (Fig. 3).

V. CONCLUSION

In conclusion, we have shown that the THz emission from spintronic THz emitters arises from three mechanisms: the spin-charge conversion, the anomalous Hall effect, and the magnetic dipole radiation. The three mechanisms show different CoFeB thickness dependences. The THz radiation generated from the spin-charge conversion is significantly reduced by inserting a thin Al_2O_3 layer in the ferromagnet/heavy metal heterojunctions. It is found that spin-charge conversion is suppressed if the Al_2O_3 thickness is above 1 nm. Our experiment reveals the interplay of the spintronic THz emission mechanisms in spintronic THz emitters. Using the magnetic dipole radiation as a reference signal, it is possible to evaluate the ultrafast electric current pulses in spintronics THz emitters.

ACKNOWLEDGMENTS

Y.X. would like to thank Stéphane Mangin, Grégory Malinowski, and Michel Hehn for the fruitful discussion. The authors gratefully acknowledge the National Natural Science Foundation of China (Grants No. 11904016, No. 12004025, and No. 61627813), and Beihang Hefei Innovation Research Institute Project (Grants No. BHKX-19-01 and No. BHKX-19-02). All the authors sincerely thank Hefei Truth Equipment Co., Ltd. for the help on film deposition.

APPENDIX A: THIN-FILM ROUGHNESS

To quantify the roughness of the Al_2O_3 layer, we performed the AFM analysis for Glass//Al_2O_3 (3 nm). The film height is found to vary between -0.4 nm and $+0.4$ nm. (Fig. 7).

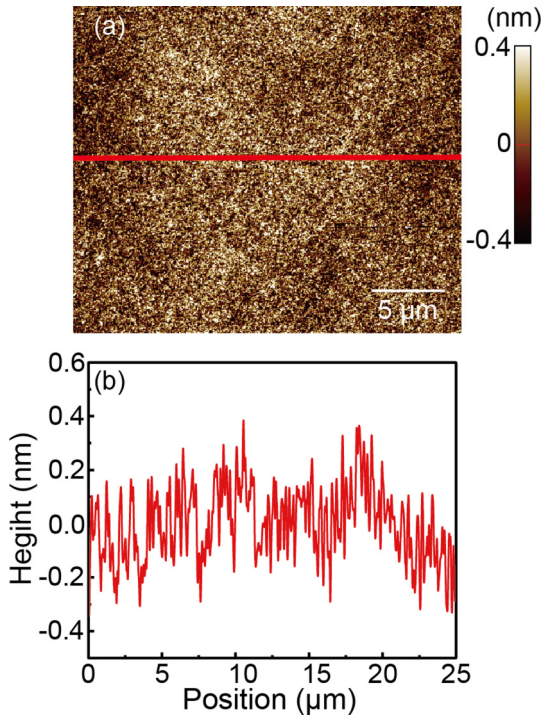

FIG. 7. (a) A typical AFM image of glass//Al_2O_3 (3 nm) film. (b) Height profile extracted at the red line, showing a step height of ~0.8 nm.

APPENDIX B: ULTRAFAST DEMAGNETIZATION

We analyzed the ultrafast demagnetization dynamics of CoFeB [Fig. 8(a)]. The magnetic current density can be evaluated using the ultrafast demagnetization curve [Fig. 8(b)]. For the laser fluence used in this study (0.42 mJ/cm^2), we observe 40% demagnetization, which corresponds to a peak magnetic current density of 3.8×10^{11} V/m^2.

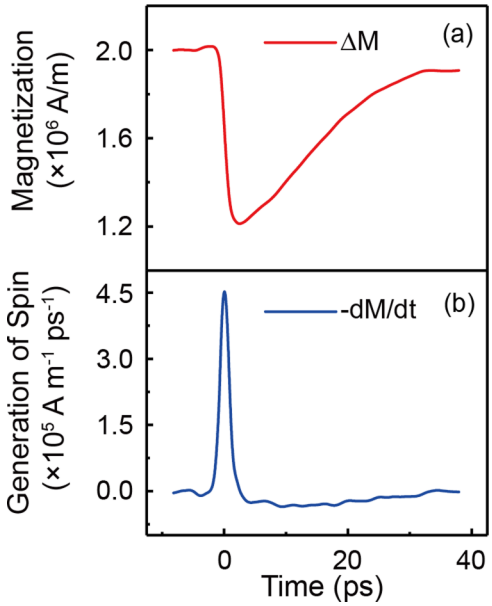

FIG. 8. (a) The ultrafast demagnetization curve was measured via the time-resolved magneto-Kerr effect. (b) In the CoFeB layer, the spin generation rate per unit volume is obtained by numerical differentiation of the demagnetization curve.

APPENDIX C: ULTRAFAST SPIN DIFFUSION

Figure 9 shows the spin diffusion in the ferromagnet/heavy metal heterostructure calculated using the spin diffusion model.

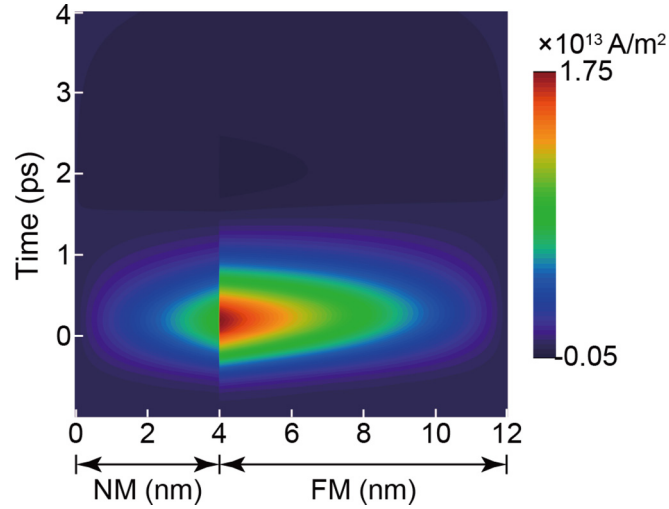

FIG. 9. Calculated spin-current dynamics in the ferromagnet and heavy metal layers with respect to time.

[1] E. Beaurepaire, J. Merle, A. Daunois, and J. Bigot, Ultrafast Spin Dynamics in Ferromagnetic Nickel, Phys. Rev. Lett. **76**, 4250 (1996).

[2] B. Koopmans, G. Malinowski, F. Dalla Longa, D. Steiauf, M. Fahnle, T. Roth, M. Cinchetti, and M. Aeschlimann, Explaining the paradoxical diversity of ultrafast laser-induced demagnetization, Nat. Mater. **9**, 259 (2010).

[3] N. Bergeard, M. Hehn, S. Mangin, G. Lengaigne, F. Montaigne, M. L. Lalieu, B. Koopmans, and G. Malinowski, Hot-Electron-Induced Ultrafast Demagnetization in Co/Pt Multilayers, Phys. Rev. Lett. **117**, 147203 (2016).

[4] G. Malinowski, F. Dalla Longa, J. H. H. Rietjens, P. V. Paluskar, R. Huijink, H. J. M. Swagten, and B. Koopmans, Control of speed and efficiency of ultrafast demagnetization by direct transfer of spin angular momentum, Nat. Phys. **4**, 855 (2008).

[5] W. Zhang, P. Maldonado, Z. Jin, T. S. Seifert, J. Arabski, G. Schmerber, E. Beaurepaire, M. Bonn, T. Kampfrath, P. M. Oppeneer, and D. Turchinovich, Ultrafast terahertz magnetometry, Nat. Commun. **11**, 4247 (2020).

[6] E. Beaurepaire, G. M. Turner, S. M. Harrel, M. C. Beard, J. Y. Bigot, and C. A. Schmuttenmaer, Coherent terahertz emission from ferromagnetic films excited by femtosecond laser pulses, Appl. Phys. Lett. **84**, 3465 (2004).

[7] K. Neeraj, N. Awari, S. Kovalev, D. Polley, N. Z. Hagström, S. S. P. K. Arekapudi, A. Semisalova, K. Lenz, B. Green, and J.-C. Deinert, Inertial spin dynamics in ferromagnets, Nat. Phys. **17**, 245 (2021).

[8] R. Schneider, M. Fix, J. Bensmann, S. Michaelis de Vasconcellos, M. Albrecht, and R. Bratschitsch, Spintronic GdFe/Pt THz emitters, Appl. Phys. Lett. **115**, 152401 (2019).

[9] H. Qiu, L. Zhou, C. Zhang, J. Wu, Y. Tian, S. Cheng, S. Mi, H. Zhao, Q. Zhang, and D. Wu, Ultrafast spin current generated from an antiferromagnet, Nat. Phys. **17**, 388 (2021).

[10] L. Huang, J.-W. Kim, S.-H. Lee, S.-D. Kim, V. M. Tien, K. P. Shinde, J.-H. Shim, Y. Shin, H. J. Shin, S. Kim, J. Park, S.-Y. Park, Y. S. Choi, H.-J. Kim, J.-I. Hong, D. E. Kim, and D.-H. Kim, Direct observation of terahertz emission from ultrafast spin dynamics in thick ferromagnetic films, Appl. Phys. Lett. **115**, 142404 (2019).

[11] T. Kampfrath, M. Battiato, P. Maldonado, G. Eilers, J. Nötzold, S. Mährlein, V. Zbarsky, F. Freimuth, Y. Mokrousov, S. Blügel, M. Wolf, I. Radu, P. M. Oppeneer, and M. Münzenberg, Terahertz spin current pulses controlled by magnetic heterostructures, Nat. Nanotechnol. **8**, 256 (2013).

[12] R. Schneider, M. Fix, R. Heming, S. Michaelis de Vasconcellos, M. Albrecht, and R. Bratschitsch, Magnetic-field-dependent

THz emission of spintronic TbFe/Pt layers, ACS Photonics **5**, 3936 (2018).

[13] M. Battiato, K. Carva, and P. M. Oppeneer, Superdiffusive Spin Transport as a Mechanism of Ultrafast Demagnetization, Phys. Rev. Lett. **105**, 027203 (2010).

[14] A. Melnikov, I. Razdolski, T. O. Wehling, E. T. Papaioannou, V. Roddatis, P. Fumagalli, O. Aktsipetrov, A. I. Lichtenstein, and U. Bovensiepen, Ultrafast Transport of Laser-Excited Spin-Polarized Carriers in Au/Fe/MgO (001), Phys. Rev. Lett. **107**, 076601 (2011).

[15] G. M. Choi, B. C. Min, K. J. Lee, and D. G. Cahill, Spin current generated by thermally driven ultrafast demagnetization, Nat. Commun. **5**, 4334 (2014).

[16] G. M. Choi and D. G. Cahill, Kerr rotation in Cu, Ag, and Au driven by spin accumulation and spin-orbit coupling, Phys. Rev. B **90**, 214432 (2014).

[17] A. Eschenlohr, M. Battiato, P. Maldonado, N. Pontius, T. Kachel, K. Holldack, R. Mitzner, A. Föhlisch, P. M. Oppeneer, and C. Stamm, Ultrafast spin transport as key to femtosecond demagnetization, Nat. Mater. **12**, 332 (2013).

[18] D. M. Nenno, B. Rethfeld, and H. C. Schneider, Particle-in-cell simulation of ultrafast hot-carrier transport in Fe/Au heterostructures, Phys. Rev. B **98**, 224416 (2018).

[19] G. Li, R. Medapalli, R. Mikhaylovskiy, F. Spada, T. Rasing, E. Fullerton, and A. Kimel, THz emission from Co/Pt bilayers with varied roughness, crystal structure, and interface intermixing, Phys. Rev. Mater. **3**, 084415 (2019).

[20] T. Seifert *et al.*, Efficient metallic spintronic emitters of ultrabroadband terahertz radiation, Nat. Photonics **10**, 483 (2016).

[21] Y. Wu, M. Elyasi, X. Qiu, M. Chen, Y. Liu, L. Ke, and H. Yang, High-performance THz emitters based on ferromagnetic/nonmagnetic heterostructures, Adv. Mater. **29**, 1603031 (2017).

[22] C. Zhou, Y. Liu, Z. Wang, S. Ma, M. W. Jia, R. Wu, L. Zhou, W. Zhang, M. Liu, and Y. Wu, Broadband Terahertz Generation Via the Interface Inverse Rashba-Edelstein Effect, Phys. Rev. Lett. **121**, 086801 (2018).

[23] M. B. Jungfleisch, Q. Zhang, W. Zhang, J. E. Pearson, R. D. Schaller, H. Wen, and A. Hoffmann, Control of Terahertz Emission by Ultrafast Spin-Charge Current Conversion at Rashba Interfaces, Phys. Rev. Lett. **120**, 207207 (2018).

[24] X. Wang, L. Cheng, D. Zhu, Y. Wu, M. Chen, Y. Wang, D. Zhao, C. B. Boothroyd, Y. M. Lam, and J. X. Zhu, Ultrafast Spin-to-charge conversion at the surface of topological insulator thin films, Adv. Mater. **30**, 1802356 (2018).

[25] J. Cramer, T. Seifert, A. Kronenberg, F. Fuhrmann, G. Jakob, M. Jourdan, T. Kampfrath, and M. Kläui, Complex terahertz and direct current inverse spin hall effect in YIG/Cu1–x Ir x bilayers across a wide concentration range, Nano Lett. **18**, 1064 (2018).

[26] K. Shen, G. Vignale, and R. Raimondi, Microscopic Theory of the Inverse Edelstein Effect, Phys. Rev. Lett. **112**, 096601 (2014).

[27] X. Chen, X. Wu, S. Shan, F. Guo, D. Kong, C. Wang, T. Nie, C. Pandey, L. Wen, W. Zhao, C. Ruan, J. Miao, Y. Li, and L. Wang, Generation and manipulation of chiral broadband terahertz waves from cascade spintronic terahertz emitters, Appl. Phys. Lett. **115**, 221104 (2019).

[28] T. J. Huisman, R. V. Mikhaylovskiy, J. D. Costa, F. Freimuth, E. Paz, J. Ventura, P. P. Freitas, S. Blügel, Y. Mokrousov, T. Rasing, and A. V. Kimel, Femtosecond control of electric currents in metallic ferromagnetic heterostructures, Nat. Nanotechnol. **11**, 455 (2016).

[29] R. Medapalli, D. Afanasiev, D. Kim, Y. Quessab, S. Manna, S. Montoya, A. Kirilyuk, T. Rasing, A. V. Kimel, and E. E. Fullerton, Multiscale dynamics of helicity-dependent all-optical magnetization reversal in ferromagnetic Co/Pt multilayers, Phys. Rev. B **96**, 224421 (2017).

[30] Q. Zhang, Z. Luo, H. Li, Y. Yang, X. Zhang, and Y. Wu, Terahertz Emission from Anomalous Hall Effect in a Single-Layer Ferromagnet, Phys. Rev. Appl. **12**, 054027 (2019).

[31] G. Torosyan, S. Keller, L. Scheuer, R. Beigang, and E. T. Papaioannou, Optimized spintronic terahertz emitters based on epitaxial grown Fe/Pt layer structures, Sci. Rep. **8**, 1311 (2018).

[32] O. Panahi, B. Yahyaei, S. M. Mousavi, and A. M. Ghiasabadi, High performance terahertz emitter based on inverse spin Hall effect in metallic Fe/Au heterostructure, Laser Phys. **30**, 055001 (2020).

[33] T. Seifert, S. Jaiswal, M. Sajadi, G. Jakob, S. Winnerl, M. Wolf, M. Kläui, and T. J. A. P. L. Kampfrath, Ultrabroadband single-cycle terahertz pulses with peak fields of 300 kV cm−1 from a metallic spintronic emitter, Appl. Phys. Lett. **110**, 252402 (2017).

[34] D. Yang, J. Liang, C. Zhou, L. Sun, R. Zheng, S. Luo, Y. Wu, and J. Qi, Powerful and tunable THz emitters based on the Fe/Pt magnetic heterostructure, Adv. Opt. Mater. **4**, 1944 (2016).

[35] C. F. Pai, L. Liu, Y. Li, H. Tseng, D. Ralph, and R. Buhrman, Spin transfer torque devices utilizing the giant spin Hall effect of tungsten, Appl. Phys. Lett. **101**, 122404 (2012).